



CHORUS

This is the accepted manuscript made available via CHORUS. The article has been published as:

Strong correlations between vacancy and magnetic ordering in superconducting $K_{0.8}Fe_{2-y}Se_2$

J. Yang, C. Duan, Q. Huang, C. Brown, J. Neufeind, and Despina Louca

Phys. Rev. B **94**, 024503 — Published 5 July 2016

DOI: [10.1103/PhysRevB.94.024503](https://doi.org/10.1103/PhysRevB.94.024503)

Strong correlations between vacancy and magnetic ordering in superconducting $\text{K}_{0.8}\text{Fe}_{2-y}\text{Se}_2$

J. Yang,¹ C. Duan,¹ Q. Huang,² C. Brown,² J. Neufeind,³ Despina Louca^{1*}

¹*University of Virginia, Charlottesville, VA 22904, USA.*

²*NIST Center for Neutron Research, Gaithersburg, MD 20899, USA and*

³*Oak Ridge National Laboratory, Oak Ridge, TN 37831, USA.*

(Dated: June 17, 2016)

The coexistence of magnetic and non-magnetic phases in the superconducting potassium iron selenide, $\text{K}_x\text{Fe}_{2-y}\text{Se}_2$, has been intensely debated. With superconductivity proposed to appear in a stoichiometric, non-magnetic phase with the I_4/mmm crystal symmetry, the proposed non-superconducting phase is magnetic and with a lower symmetry, I_4/m . The latter consists of Fe vacancies that go through a disordered to an ordered transition in which the partially filled Fe sites create a supercell upon ordering. We show using neutron scattering on the optimally doped composition, $\text{K}_{0.8}\text{Fe}_{2-y}\text{Se}_2$, that the absence of magnetism does not signal the presence of superconductivity. Moreover, the degree of vacancy order is coupled to the strength of the magnetic order. Superconductivity coincides with the presence of the magnetic order parameter, albeit the latter significantly weaker than previously reported, contradicting the current understanding of this ~ 30 K superconductor.

PACS numbers: 61.05.F-, 74.62.Dh, 74.70.Ad, 75.50.Bb

INTRODUCTION

When potassium, K, is intercalated between the tetrahedral layers of the binary chalcogenide superconductor, Fe_{1-y}Se ($T_C \sim 8$ K), the superconducting transition temperature, T_C , shows a fourfold increase [1–7]. The $\text{K}_x\text{Fe}_{2-y}\text{Se}_2$ phase diagram is quite complex. Vacancies are present at the K and Fe sites, while the latter undergoes a disorder to an order transition at $T_S \sim 580$ K [2] upon cooling. Above this temperature, the symmetry is I_4/mmm in which only one Fe site is present and the Fe vacancies are randomly distributed in the lattice. What happens to the lattice below T_S has been quite controversial with several scenarios proposed. It has been suggested that a stoichiometric phase with the I_4/mmm high temperature symmetry persists below T_S concomitantly with the emergence of a non-stoichiometric phase with a lower symmetry, I_4/m , in which the Fe vacancies undergo long-range order. The latter crystal structure is shown in Fig. 1(a) while the I_4/mmm symmetry is the same as the one found in the BaFe_2As_2 Fe-based superconductor. Also reported is the possibility of a structural transition to the new vacancy ordered state, without the presence of the I_4/mmm high temperature phase [3, 8–11]. Moreover, an antiferromagnetic transition occurs following the structural one at $T_N \sim 560$ K [7]. Superconductivity appears in a narrow range of K intercalation, in a phase that was previously proposed to exhibit a large magnetic moment, over $3\mu_B/\text{Fe}$ atom, a non-trivial quantity, and much larger than what is found in other Fe-based compounds [3]. A long standing issue in this system has been whether or not such strong magnetic coupling is

viable in the superconducting state, and whether competing interactions lead to phase separation of the superconducting non-magnetic from the non-superconducting magnetic domains [4, 12–20].

At the center of the problem is the distribution of Fe vacancies and magnetic moments because of their possible role in the superconducting mechanism [21–28]. Several superlattice structures have been proposed for the long-range order of the Fe vacancies, including the $\sqrt{5}x\sqrt{5}x1$ [2, 3, 8, 29] (referred to as the “245” structure), $\sqrt{2}x\sqrt{2}x1$ [2, 10], $\sqrt{2}x2\sqrt{2}x1$ [2, 7, 30] and $\sqrt{8}x\sqrt{10}x1$ [4] types. Does the superconducting state appear in a minority phase devoid of a superlattice structure, as suggested from scanning tunneling [21], nuclear magnetic resonance [31] and transmission electron microscopy measurements [7]? If a stoichiometric KFe_2Se_2 (122 composition) is phase separated from the vacancy ordered matrix however, it implies a superconductive phase that is heavily electron doped [4, 21, 32, 33]. Theoretical calculations have shown that in the “245” $\text{K}_x\text{Fe}_{2-y}\text{Se}_2$ structure, disorder can suppress the band structure reconstruction without destroying the Fermi surface, while it raises the chemical potential eliminating the hole pockets, in agreement with ARPES results [33, 34]. Thus it is hypothesized that the degree of vacancy order is strongly coupled to Cooper pair formation and scattering. To this end, the crystal structure is revisited to investigate the structure-property relationship in this Fe-based superconductor.

Via the systematic growth of single crystals of $\text{K}_{0.8}\text{Fe}_{2-y}\text{Se}_2$, we find that the distribution of Fe vacancies, the crystal structure and its magnetism are strongly

interrelated with the superconducting volume fraction. Here, four growth conditions are compared: one in which crystals are grown in sealed quartz tubes filled with Ar and slow cooled to room temperature; another in which crystals are grown in vacuum sealed quartz tubes and slow cooled to room temperature; a third in which the Ar grown crystals undergo further annealing in Ar gas at 350 °C and then quenched; and a fourth in which the vacuum grown crystals are further annealed in vacuum also at 350 °C and quenched to room temperature. Similar growth conditions have been reported in Refs. [4, 13, 35–37].

SAMPLE PREPARATION AND CHARACTERIZATION

The single crystalline of $K_xFe_{2-y}Se_2$ were grown by self-flux method. First, high-purity tetragonal FeSe powders were synthesized using solid-state reaction method. Stoichiometric quantities of iron pieces (Alfa Aesar, 99.99%) and selenium powder (Alfa Aesar, 99.999%) were weighted and sealed in vacuum quartz tubes. The samples were heated to 1075 °C for 30 h, then annealed at 400 °C for 50 h, and finally quenched to liquid nitrogen. The K grain and FeSe powders with a nominal composition of K: FeSe = 0.8: 2 were placed in an alumina crucible and double sealed into quartz tubes partially backfilled with ultrahigh-purity argon. All the weighing, mixing, grinding and pressing procedures were performed in a glove box under argon atmosphere with the oxygen and moisture below 1 p.p.m. The samples grown in vacuum were double sealed into high vacuum quartz tubes evacuated by a molecular pump. All samples were heated at 1030 °C for 2 h and cooled down to 750 °C with a rate of 6 °C/h, and then they were cooled to room temperature by switching off the power of the furnace. High quality single crystals were mechanically cleaved from the solid chunks in the glove box. Finally, the as grown single crystals were thermally treated for 2 hours at 350 °C and followed by quenching in liquid nitrogen. The single crystals grown in partially backfilled argon were thermally treated in partially backfilled argon, and the single crystals grown in vacuum were thermally treated in vacuum. The actual compositions are $K_{0.74(8)}Fe_{1.70(8)}Se_2$ for the vacuum as grown sample, $K_{0.78(4)}Fe_{1.74(5)}Se_2$ for the vacuum annealed sample and $K_{0.75(6)}Fe_{1.69(6)}Se_2$ for the argon annealed sample respectively, which were determined by inductively coupled plasma optical emission spectroscopy (ICP-OES). The DC magnetic susceptibilities were measured using the Quantum design PPMS in the temperature range from 2 to 300 K. Neutron powder diffraction measurements were performed using the BT1 diffractometer at the NIST Center for Neutron Research (NCNR) in Gaithersburg, Maryland, with the neutron wavelength of $\lambda = 2.078 \text{ \AA}$ at 10 K. The pair density

function (PDF) was determined from the neutron data collected at the NOMAD diffractometer at the Spallation Neutron Source of Oak Ridge National Laboratory as a function of temperature, from 2 to 300 K. The single crystals were ground into powder inside a helium-filled glove box prior to the experiment.

First we describe the bulk transport and magnetization measurements. Fig. 1(b) is a plot of the bulk magnetization, $4\pi\chi$, for zero-field cooled (ZFC) and field-cooled (FC) measurements for the crystals grown in Ar gas. The red squares correspond to the quenched as grown crystals (AG-Ar) while the blue dots correspond to the crystals that were subsequently annealed in Ar (Ar-anneal). Fig. 1(c) is a similar plot that compares the temperature dependence of $4\pi\chi$ of the as-grown crystal grown in vacuum (AG-Va - red squares) to a crystal from the same batch but with subsequent annealing in vacuum (Va-anneal - blue dots). It can readily be seen that the as-grown crystals are either marginally or not at all superconducting and show a bad connectivity of the superconducting grains. On the other hand, the annealed crystals in vacuum or Ar gas show significant enhancement of the percent diamagnetic signal. In the case for the Ar-anneal crystals, it reaches close to 75 % of full diamagnetism while the Va-anneal crystals reach about 50 %. A heat capacity measurement as as-grown samples reported in Ref. [36] shows a discontinuity at T_C , indicating that the superconductivity is bulk. Chemical analysis yielded a very similar chemical composition for the two highest shielding fraction crystals: a composition of $K_{0.76}Fe_{1.70}Se_2$ for the Ar-anneal and $K_{0.78}Fe_{1.74}Se_2$ for the Va-anneal. For comparison, in the AG-Va crystal which exhibits a small negative $4\pi\chi$ value at the lowest temperature, the chemical composition is $K_{0.74(8)}Fe_{1.70(8)}Se_2$. Shown in Fig. 1(d) is the resistivity, $\rho(T)$, in units of $\Omega.cm$. A broad hump indicating a semiconducting to metal cross-over is observed around 200 K, followed by the superconducting transition at ~ 31 K [1, 4]. The back-scattered electron images of scanning electron microscopy (SEM) were measured on cleaved surfaces of Ar-as-grown (AG-Ar) and Ar-annealed (Ar-anneal) samples and are shown in Fig. 2. Fig. 2(a) and (b) exhibit the results of the AG-Ar sample. Clearly the surface separates into two kinds of regions: domains with brighter color and rectangular shape, buried in the background of darker regions. However, as shown in Figs. 2(c) and (d), the brighter rectangular domains were not observed in the Ar-anneal sample. Instead, very tiny bright dots were observed in the Ar-anneal sample. Furthermore, different from previous reports that the brighter domains were changed to smaller but connecting chains in the annealed sample, we do not see obvious connecting chains on our Ar-anneal sample, even at the highest resolution as shown in Fig. 2(d). In this case, the enhancement of the superconducting shielding fraction of Ar-anneal sample is not due to the connectivity of the minority phase. The results on

the annealed crystal are somewhat different from those reported in Ref. [4].

The neutron diffraction data collected using the BT1 diffractometer at the NIST Center for Neutron Research suggest that all crystals have some magnetic component i.e. magnetic peaks are present in all as seen in the three panels of Fig. 3, albeit with varying intensity and much smaller than previously reported [2, 3]. The magnetic peaks can only be indexed in the $I4/m$ symmetry. Moreover, the refined moments are nowhere near as large as previous reports stated [2, 3]. The results from the refinement are summarized in Table I. From the data refinement, it is deduced that in the marginal superconductors, very weak magnetism is present, if any. Thus the absence of magnetism is not indicative of a superconducting state. In the plot of Fig. 2(a), the neutron diffraction pattern collected at 2 K for the AG-Ar crystal is fit using the $I4/m$ symmetry. The magnetic peak is barely discernible as indicated, and the magnetic moment is refined to be about $0.5 \pm 0.3 \mu_B$. The same is true for the (110) Bragg peak which is from the $I4/m$ vacancy ordered structure of the $\sqrt{5} \times \sqrt{5} \times 1$ type. Most important is the fact that the Fe1 and Fe2 sites are almost equally occupied as seen in the tables provided in the supplement, with vacancies at both sites, although more at the Fe1 than at the Fe2 site. Therefore in the absence of a strong magnetic moment, both sites carry vacancies while the very weak (110) peak signifies poor vacancy ordering because the occupancy of the Fe1 and Fe2 sites is comparable. Moreover, when the Fe2 site is only partially full, superconductivity is suppressed.

With annealing, the Fe2 site occupancy reaches unity while the Fe1 site remains partially empty. Further, with the increase of the occupancy at the Fe2 site, the magnetic moment increases as well. This is because the magnetism is associated with the Fe2 site and not with the Fe1 [3, 39, 40]. The neutron data from the Ar-anneal crystal in Fig. 3(b) clearly show a more intense $(101)_M$ and $(110)_{I4/m}$ peaks than in the AG-Ar. In this case, the magnetic moment is refined to be $\sim 1.36 \pm 0.07 \mu_B$. Similarly, in the Va-anneal crystal, the magnetic moment is comparable, at $\sim 1.65 \pm 0.16 \mu_B$. However, the fraction of Fe1 site occupancy is higher in the latter compound than in the Ar anneal crystal that explains the reduction of its $(110)_{I4/m}$ superlattice peak due to fewer vacancies (Fig 3(c)). In comparison to earlier neutron measurements [3], the magnetic moment is significantly smaller and so is the superlattice peak of $(110)_{I4/m}$ from the vacancy ordering. This is because the Fe1 site is not as sparsely populated as in Ref. [3], hence there is a lower degree of vacancy ordering overall in our crystals that most likely reduces scattering and promotes superconductivity. Thus, enhancement of the superconducting connectivity is related to the higher occupancy of the Fe2 site, reduction of the degree of vacancy ordering and suppression of the magnetic moment.

The subtleties of the Fe distribution between the two sites can also be seen in the local structure as well, obtained by Fourier transforming the diffraction data collected using the high intensity powder diffractometer, NOMAD, at Oak Ridge National Laboratory. Represented by the pair density function (PDF), $\rho(r)$, the local atomic structure is a superposition of the atomic correlations regardless of symmetry or periodicity [41]. The PDF's shown in Fig. 4(a) are from data collected on the same crystals. The first peak corresponds to Fe-Se correlations within the tetrahedron, which is the shortest bond in the unit cell, while the second corresponds to Fe-Fe correlations as reported elsewhere [39, 42]. The fluctuations of the $\rho(r)$ correspond to local atomic variations present in the different crystals, with clear differences observed between the samples prepared in vacuum (left panel) and the ones prepared in Ar gas (right panel). The Fe-Fe double peak feature present in all compounds cannot be reproduced by a model PDF calculated based on the $I4/mmm$ symmetry [39] and shown as the dashed line in Fig. 4(b).

The best fit to the local environment is obtained when the $I4/m$ symmetry is assumed. Given that within the $I4/m$ there are two Fe sites, there are three kinds of bond pairs contributing to the Fe correlation peak, from Fe1-Fe1, Fe1-Fe2, and Fe2-Fe2. The presence of short and long Fe-Fe bonds in the region from 2.6 to 3.0 Å is from the superposition of the three pairs. The multiplicity at the Fe2 site is 16 while at the Fe1 site it is 4, thus the area under the two peaks is scaled proportionately. To contrast with the $I4/mmm$ symmetry in which only one Fe site is present, with an Fe-Fe bond length at ~ 2.8 Å as shown in Fig. 4(b), the double-peak feature observed in the data of all samples is a signature of the $I4/m$. This analysis cannot exclude the possibility of the presence of small quantities (less than 5 %) of the $I4/mmm$ structure. Note that the weight distribution between the double peak feature is different from crystal to crystal, which is a reflection of the different Fe and K distributions, and the Fe vacancies, as discussed above. At the same time, the susceptibility data of Fig. 1 show clear differences between samples that have been annealed or not. Thus one would expect that if a stoichiometric $I4/mmm$ associated with superconductivity phase separates, it would become more prominent in the annealed samples. Instead, what is observed is a redistribution of the Fe bonds within the same symmetry. This is discussed next.

The local geometry is governed by the K2, Fe2 and Se1/2 coordinates while the Fe1 and K1 coordinates are fixed by the $I4/m$ symmetry. The initial atom parameters used to calculate a local model are obtained from the crystal refinement. These values are subsequently modified to best fit the $\rho(r)$. The parameters are listed in Table II. The results from the fitting are shown in Fig. 4(b) where the data (black symbols) for the Ar-anneal sample is compared to a local model (solid red

line). In this model, a double unit cell is assumed with two local Fe2 environments. The two environments are shown in Fig. 4(c) which are plots of the FeSe sub-lattice projected on the ab-plane. The square plaquette at the center of each unit is contracted in the local environment (LE) LE-I and expanded in LE-II, resulting in two unique environments as shown in the figure. The superposition of the two unit cells results in an overall fitting that is the red solid line of Fig. 4(b). The model, which also includes 5 % excess Fe, can fit the data well especially in the region of the Fe correlations. Similar models have been obtained for the other samples as well. Also shown in this figure are the partial functions calculated from this model for the Fe2-Fe2 and Fe2-Fe1 correlations that show the distribution of the bonds. Note that the bonds between Fe1-Fe1 atoms do not contribute in this region at all. The presence of the two local environments around Fe may be related to the amount of Fe1 vacancies in the immediate vicinity. As the ratio of LE-I to LE-II changes from sample to sample so does the distribution of vacancies that in turn affects connectivity between the superconducting regions.

In summary, the complex lattice landscape resulting from competing magnetic and superconducting phases, is a phenomenon commonly observed in complex superconducting systems such as in cuprates, bismuth perovskites, cobaltates and more recently in H_2S . The complex local structure of $\text{K}_x\text{Fe}_{2-y}\text{Se}_2$ is manipulated by varying the growth conditions with the result of producing different phases leading to different responses. The distribution of Fe, its magnetism and the vacancies are strongly related to the connectivity of the superconducting grains with annealing. The Fe environment sensitively reflects the emergent complexity in this class of Fe-based superconductors.

The authors would like to acknowledge valuable discussions with W. Bao, T. Egami, A. Bianconi, and W. Ku. The work at the University of Virginia is supported by the U. S. Department of Energy, Office of Basic Energy Sciences and at Oak Ridge National Laboratory by the Office of Basic Energy Sciences, Division of Scientific User Facilities. The work at NIST is supported by the U. S. Department of Commerce.

Table I: The refinement results from the Rietveld analysis for (a) the AG-Ar, (b) the Ar-annealed, and (c) the Vacuum-annealed samples. The coordinates for K1 are (0,0,0), for K2 (x, y, 0), for Fe1 is $(0, \frac{1}{2}, \frac{1}{4})$, for Fe2 $(x, y, \frac{1}{4})$, for Se1 $(\frac{1}{2}, \frac{1}{2}, z)$ and for Se2 (x, y, z).

(a)	a = b = 8.652 Å, c = 14.046 Å	Uiso (Å ²)	Occ.
	$\chi^2=2.278$, $wR_p=0.057$, $R_p=0.045$		
K1		0.020	0.756
K2	x = 0.337, y = 0.199	0.020	0.756
Fe1		0.044	0.512
Fe2	x = 0.198, y = 0.095	0.044	0.829
Se1	z = 0.144	0.006	1.000
Se2	x = 0.122, y = 0.318, z = 0.145	0.006	1.000
(b)	a = b = 8.671 Å, c = 14.029 Å	Uiso (Å ²)	Occ.
	$\chi^2=1.304$, $wR_p=0.060$, $R_p=0.047$		
K1		0.020	0.835
K2	x = 0.337, y = 0.199	0.020	0.835
Fe1		0.029	0.350
Fe2	x = 0.198, y = 0.095	0.029	1.000
Se1	z = 0.144	0.010	1.000
Se2	x = 0.122, y = 0.318, z = 0.145	0.010	1.000
(c)	a = b = 8.648 Å, c = 14.029 Å	Uiso (Å ²)	Occ.
	$\chi^2=2.139$, $wR_p=0.069$, $R_p=0.054$		
K1		0.020	0.836
K2	x = 0.337, y = 0.199	0.020	0.836
Fe1		0.020	0.528
Fe2	x = 0.198, y = 0.095	0.020	1.000
Se1	z = 0.144	0.004	1.000
Se2	x = 0.122, y = 0.318, z = 0.145	0.004	1.000

Table II: The unit cell parameters for the two local environments in $\text{K}_{0.8}\text{Fe}_{2-y}\text{Se}_2$ that can describe the Fe-Fe correlations in the local lattice of Ar-annealed sample.

	Local Environment I (LE-I)				Local Environment II			
	a=8.6929 Å, c=14.016 Å				a=8.8389 Å, c=13.89 Å			
	x	y	z	Occ.	x	y	z	Occ.
K1	0	0	0	0.835	0	0	0	0.835
K2	0.3995	0.197	0	0.835	0.404	0.178	0	0.835
Fe1	0	0.5	0.25	0.35	0	0.5	0.25	0.35
Fe2	0.2	0.089	0.2508	1	0.209	0.09	0.2508	1
Se1	0.5	0.5	0.145	1	0.5	0.5	0.145	1
Se2	0.1147	0.294	0.142	1	0.115	0.294	0.142	1

*Corresponding author
E-mail: louca@virginia.edu

-
- [1] J. J. Guo, S. Jin, G. Wang, S. Wang, K. Zhu, T. Zhou, M. He, and Xiaolong Chen, Phys. Rev. B **82**, 180520(R) (2010).
[2] W. Bao, G. Li, Q. Huang, G. Chen, J. He, D. Wang, M. A. Green, Y. Qiu, J. Luo, and M. Wu, Chinese Phys. Lett. **30**, 027402 (2013).

- [3] W. Bao, Q. Huang, G. Chen, M. A. Green, D. Wang, J. He, and Y. QIU, Chinese Phys. Lett. **28**, 086104 (2011).
- [4] X. Ding, D. Fang, Z. Wang, H. Yang, J. Liu, Q. Deng, G. Ma, C. Meng, Y. Hu, and Hai-Hu Wen, Nature Commun. **4**, 1894 (2013).
- [5] J. J. Ying, X. F. Wang, X. G. Luo, A. F. Wang, M. Zhang, Y. J. Yan, Z. J. Xiang, R. H. Liu, P. Cheng, G. J. Ye, and X. H. Chen, Phys. Rev. B **83**, 212502 (2011).
- [6] D. M. Wang, J. B. He, T.-L. Xia, and G. F. Chen, Phys. Rev. B **83**, 132502 (2011).
- [7] Y. J. Yan, M. Zhang, A. F. Wang, J. J. Ying, Z. Y. Li, W. Qin, X. G. Luo, J. Q. Li, J. Hu, and X. H. Chen, Scientific Reports **2**, 00212 (2012).
- [8] F. Ye, S. Chi, Wei Bao, X. F. Wang, J. J. Ying, X. H. Chen, H. D. Wang, C. H. Dong, and M. H. Fang, Phys. Rev. Lett. **107**, 137003 (2011).
- [9] M.-H. Fang, H.-D. Wang, C.-H. Dong, Z.-J. Li, C.-M. Feng, J. Chen, and H. Q. Yuan, Europhys. Lett. **94**, 27009 (2011).
- [10] Z. Wang, Y. J. Song, H. L. Shi, Z. W. Wang, Z. Chen, H. F. Tian, G. F. Chen, J. G. Guo, H. X. Yang, and J. Q. Li, Phys. Rev. B. **83**, 140505(R) (2011).
- [11] A. Ricci, N. Poccia, G. Campi, B. Joseph, G. Arrighetti, L. Barba, M. Reynolds, M. Burghammer, H. Takeya, Y. Mizuguchi, Y. Takano, M. Colapietro, N. L. Saini, and A. Bianconi, Phys. Rev. B. **84**, 060511 (2011).
- [12] P. Dai, J. Hu, and E. Dagotto, Nature Phys. **8**, 709 (2012).
- [13] Y. Liu, Q. Xing, K. W. Dennis, R. W. McCallum, and T. A. Lograsso, Phys. Rev. B **86**, 144507 (2012).
- [14] L. Xie, Y. W. Yin, M. L. Teng, T. S. Su, X. G. Li, and J. Q. Li, Appl. Phys. Lett. **102**, 182601 (2013).
- [15] Z.-W. Wang, Z. Wang, Y.-J. Song, C. Ma, Y. Cai, Z. Chen, H.-F. Tian, H.-X. Yang, G.-F. Chen, and J.-Q. Li, J. Phys. Chem. C **116**, 17847 (2012).
- [16] S. Landsgesell, D. Abou-Ras, T. Wolf, D. Alber, and K. Proke, Phys. Rev. B **86**, 224502 (2012).
- [17] Y. Liu, Q. Xing, W. E. Straszheim, J. Marshman, P. Pedersen, R. McLaughlin, and T. A. Lograsso, Phys. Rev. B **93**, 064509 (2016).
- [18] K. Wang, H. Ryu, E. Kampert, M. Uhlarz, J. Warren, J. Wosnitza, and C. Petrovic, Phys. Rev. X **93**, 031018 (2014).
- [19] R. H. Yuan, T. Dong, Y. J. Song, P. Zheng, G. F. Chen, J. P. Hu, J. Q. Li, and N. L. Wang, Scientific Reports **2**, 00221 (2012).
- [20] M. Tanaka, Y. Yanagisawa, S. J. Denholme, M. Fujioka, S. Funahashi, Y. Matsushita, N. Ishizawa, T. Yamaguchi, H. Takeya, and Y. Takano, J. Phys. Soc. Jpn. **85**, 044710 (2016).
- [21] W. Li, H. Ding, P. Deng, K. Chang, C. Song, Ke He, L. Wang, X. Ma, J.-P. Hu, X. Chen, and Q.-K. Xue, Nature Phys. **8**, 126 (2012).
- [22] A. Chubukov, Annu. Rev. Condens. Matter Phys. **3**, 57 (2012).
- [23] J. Paglione and R. L. Greene, Nature Phys. **6**, 645 (2010).
- [24] I. I. Mazin, Nature **464**, 183 (2010).
- [25] K. Kuroki, S. Onari, R. Arita, H. Usui, Y. Tanaka, H. Kontani, and H. Aoki, Phys. Rev. Lett. **101**, 087004 (2008).
- [26] P. J. Hirschfeld, M. M. Korshunov, I. I. Mazin, Rep. Prog. Phys. **74**, 124508 (2011).
- [27] C. De la Cruz, Q. Huang, J. W. Lynn, J. Li, W. Ratcliff, J. L. Zarestky, H. A. Mook, G. F. Chen, J. L. Luo, N. L. Wang, and P. Dai, Nature **453**, 899 (2008).
- [28] Q. Huang, Y. Qiu, W. Bao, M. A. Green, J. W. Lynn, Y. C. Gasparovic, T. Wu, G. Wu, and X. H. Chen, Phys. Rev. Lett. **101**, 257003 (2008).
- [29] P. Zavalij, W. Bao, X. F. Wang, J. J. Ying, X. H. Chen, D. M. Wang, J. B. He, X. Q. Wang, G. F. Chen, P.-Y. Hsieh, Q. Huang, and M. A. Green, Phys. Rev. B. **83**, 132509 (2011).
- [30] S. M. Kazakov, A. M. Abakumov, S. Gonzalez, J. M. Perez-Mato, A. V. Ovchinnikov, M. V. Roslova, A. I. Boltalin, I. V. Morozov, E. V. Antipov, and G. V. Tendeloo, Chem Mater. **23**, 4311 (2011).
- [31] Y. Texier, J. Deisenhofer, V. Tsurkan, A. Loidl, D. S. Inosov, G. Friemel, and J. Bobroff, Phys. Rev. Lett. **108**, 237002 (2012).
- [32] B. Shen, B. Zeng, G. F. Chen, J. B. He, D. M. Wang, H. Yang, and H. H. Wen, Europhys. Lett. **96**, 37010 (2011).
- [33] Y. Zhang, L. X. Yang, M. Xu, Z. R. Ye, F. Chen, C. He, H. C. Xu, J. Jiang, B. P. Xie, J. J. Ying, X. F. Wang, X. H. Chen, J. P. Hu, M. Matsunami, S. Kimura, and D. L. Feng, Nature Mater **10**, 273 (2011).
- [34] T. Berlijn, P. J. Hirschfeld, W. Ku, Phys. Rev. Lett. **109**, 147003 (2012).
- [35] X. Ding, Y. Pan, H. Yang, and H.-H. Wen, Phys. Rev. B **89**, 224515(2014).
- [36] F. Han, B. Shen, Z.-Y. Wang, and H.-H. Wen, Phil. Mag. **92**, 2553 (2012).
- [37] H. Ryu, H. Lei, A. I. Frenkel, and C. Petrovic, Phys. Rev. B **85**, 224515 (2012).
- [38] D. Shoemaker, D. Y. Chung, H. Claus, M. C. Francisco, S. Avci, A. Llobet, and M. G. Kanatzidis, Phys. Rev. B **86**, 184511 (2012).
- [39] D. Louca, K. Park, B. Li, J. Neuefeind, and J. Yan, Scientific Reports **3**, 2047 (2013).
- [40] C. Duan, J. Yang, F. Ye, and D. Louca, J. Sup. Novel Magn. DOI:10.1007/s10948-015-3365-2 (2016).
- [41] B. H. Toby, T. Egami, Acta Cryst. A. **48**, 336 (1992).
- [42] D. Louca, K. Horigane, A. Llobet, R. Arita, S. Ji, N. Katayama, S. Konbu, K. Nakamura, T.-Y. Koo, P. Tong, and K. Yamada, Phys. Rev. B **81**, 134524 (2010).

Figure Captions

Fig. 1: In (a), the $I4/m$ crystal structure of $K_{0.8}Fe_{2-y}Se_2$ is shown. In (b), the temperature dependent superconducting shielding (ZFC) and Meissner (FC) fraction data for the as grown (red) and annealed (blue) single crystals grown in Ar gas at $H = 20$ Oe are shown. In (c), the temperature dependent superconducting shielding (ZFC) and Meissner (FC) fraction data for the as grown (red) and annealed (blue) for single crystals grown in vacuum at $H = 20$ Oe are shown. In (d), the temperature dependent resistivity for annealed (blue) single crystals grown in Ar gas is shown. The inserts are schematics of the experimental setup.

Fig. 2: Back-scattered electron images of SEM measurements on the cleaved surface of two typical samples. The topography of the cleaved surface of the Ar-as-grown (AG-Ar) sample. (a) scale bar of $5 \mu m$, (b) scale bar, $2 \mu m$. And the topography of the cleaved surface of the Ar-anneal sample. (c) scale bar of $5 \mu m$, (d) scale bar, $1 \mu m$. The measurements were done with the voltage of 10 kV.

Fig. 3: In (a) through (c), the neutron diffraction data collected at BT-1 of the (002) peak at 2 K for as grown in Ar gas (a), annealed in Ar gas (b) and annealed in vacuum (c) are shown. They are fit with the $I4/m$ symmetry. Indicated in the three panels are the magnetic (101) and the superlattice (110) peak that arise from the $I4/m$ symmetry. The magnetic moments are significantly reduced similarly to the superlattice peak, which suggests that vacancy ordering is quite poor.

Fig. 4: In (a), the data PDF's corresponding to the local atomic structure for the four crystals are shown. In (b), the data for the Ar-anneal crystal is fit to a local model assuming the $I4/m$ symmetry. The parameters for this model are provided in Table S4. Also included in

the model is an excess of about 5 % of pure Fe metal, a residual from the synthesis. The fitting between the experimental data and the model is quite good, especially in the region involving the Fe correlations between 2.5 and 3.0 Å. Also shown in this figure are the partial functions calculated from the model for the two most significant correlations of Fe, Fe2-Fe2 and Fe2-Fe1. Also shown in dashed line is a model assuming a local structure based on the $I4/mmm$ symmetry. The single Fe-Fe correlation is present in this symmetry that resides in between the Fe correlations observed in the experimental data. In (c), a real-space image of the Fe sublattice is shown, projected on the ab-plane that corresponds to the PDF shown in (b).

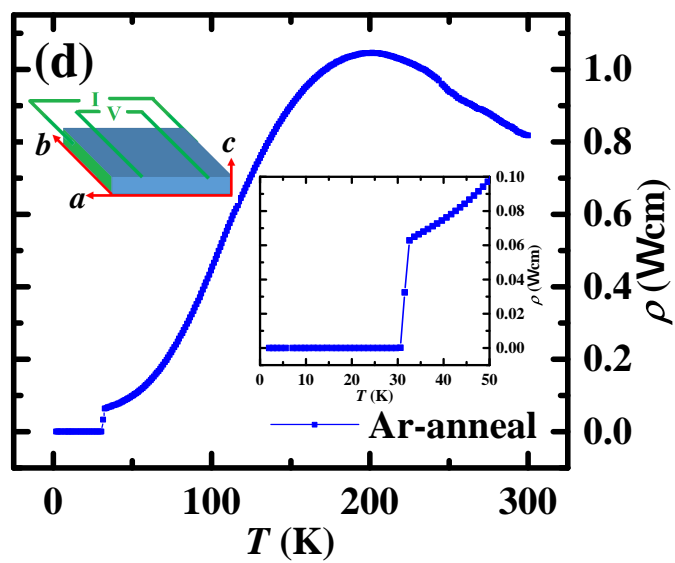
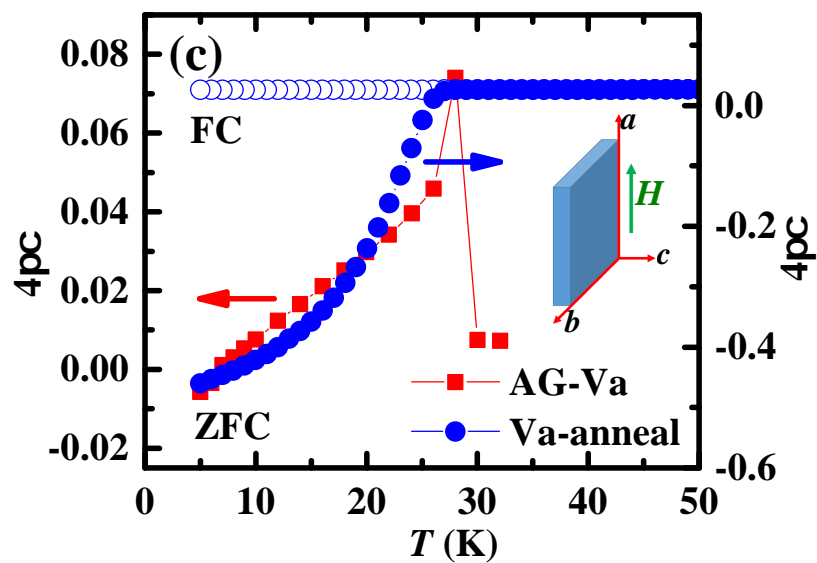
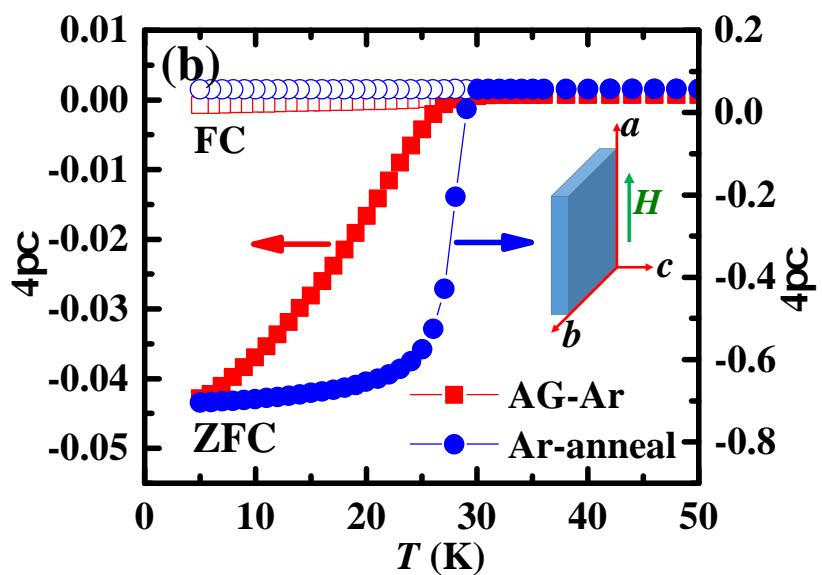
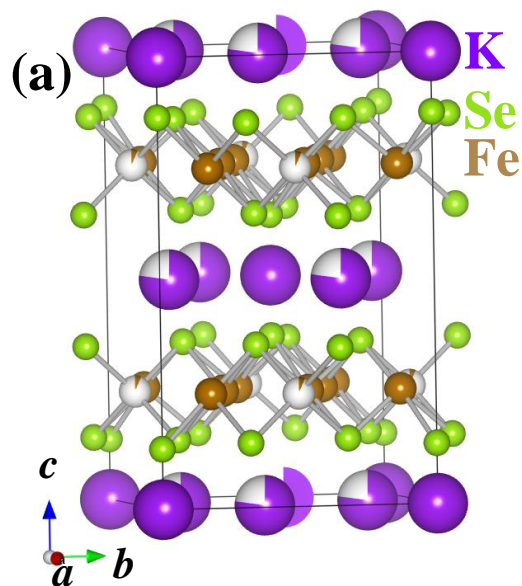
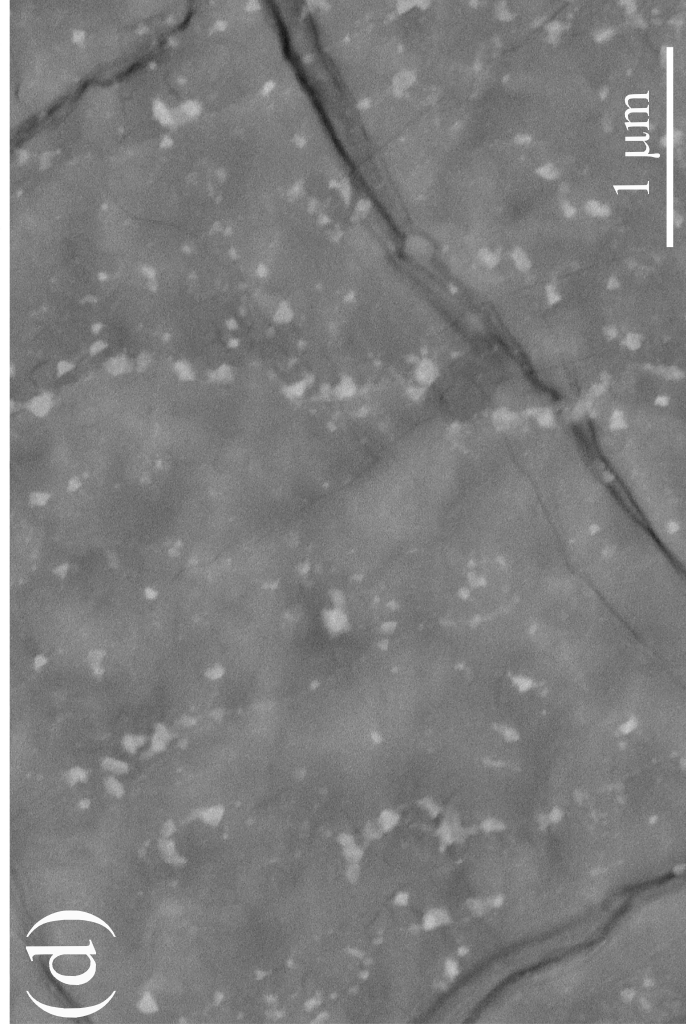
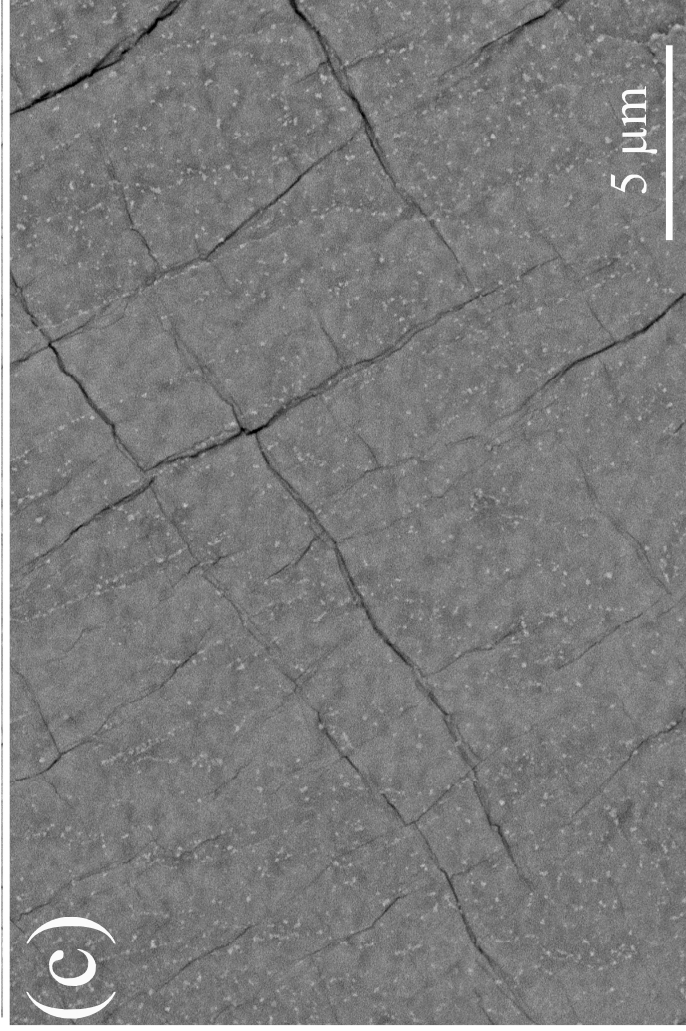
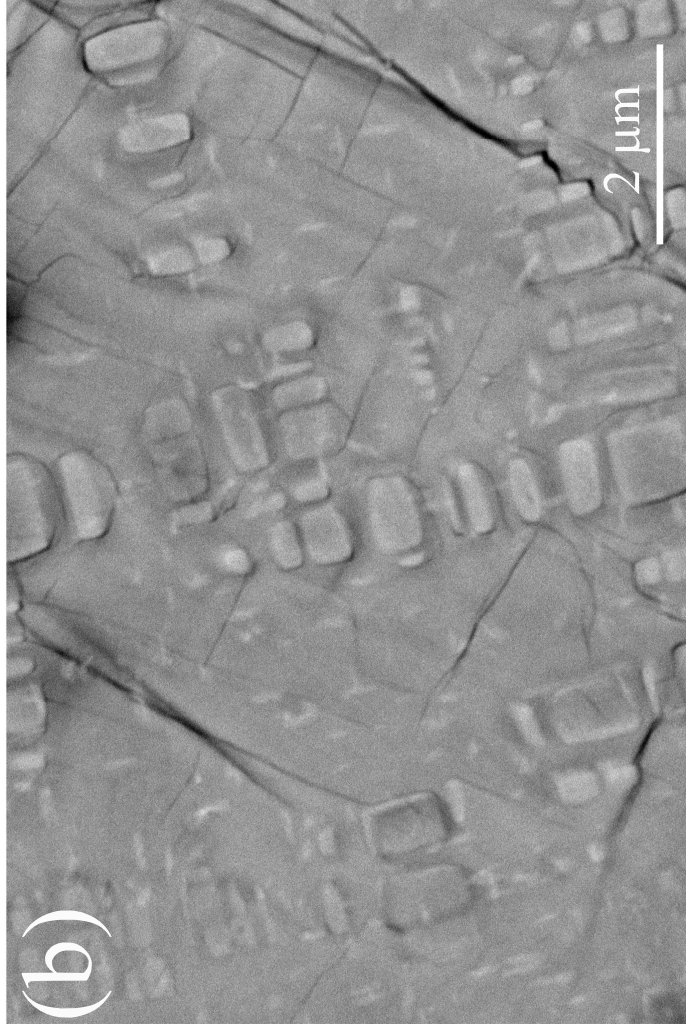
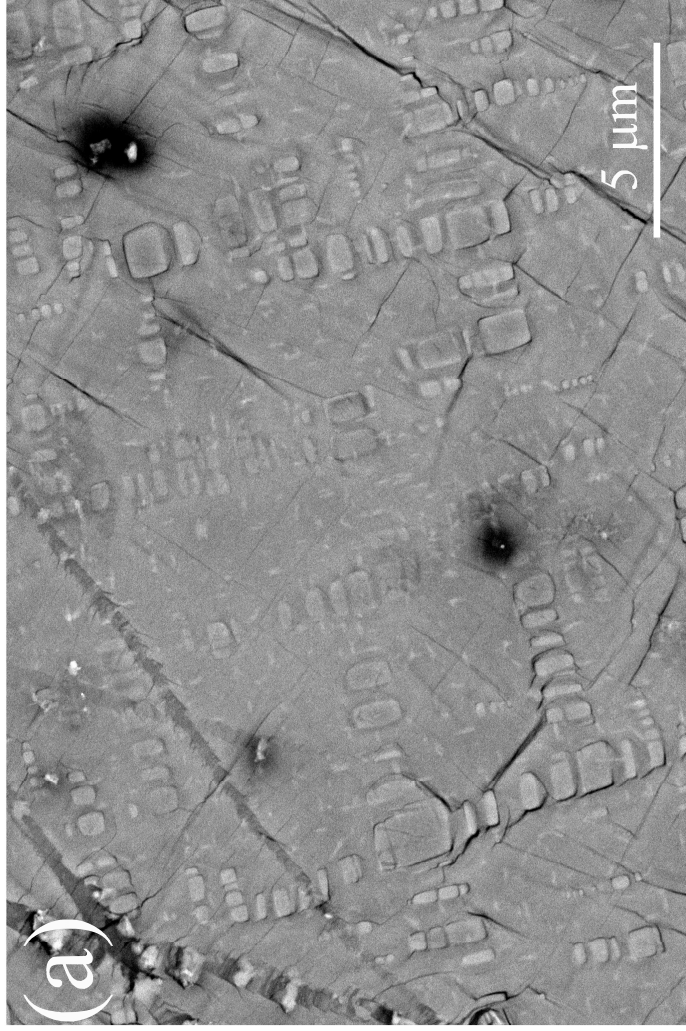


Figure 1, Yang *et al*



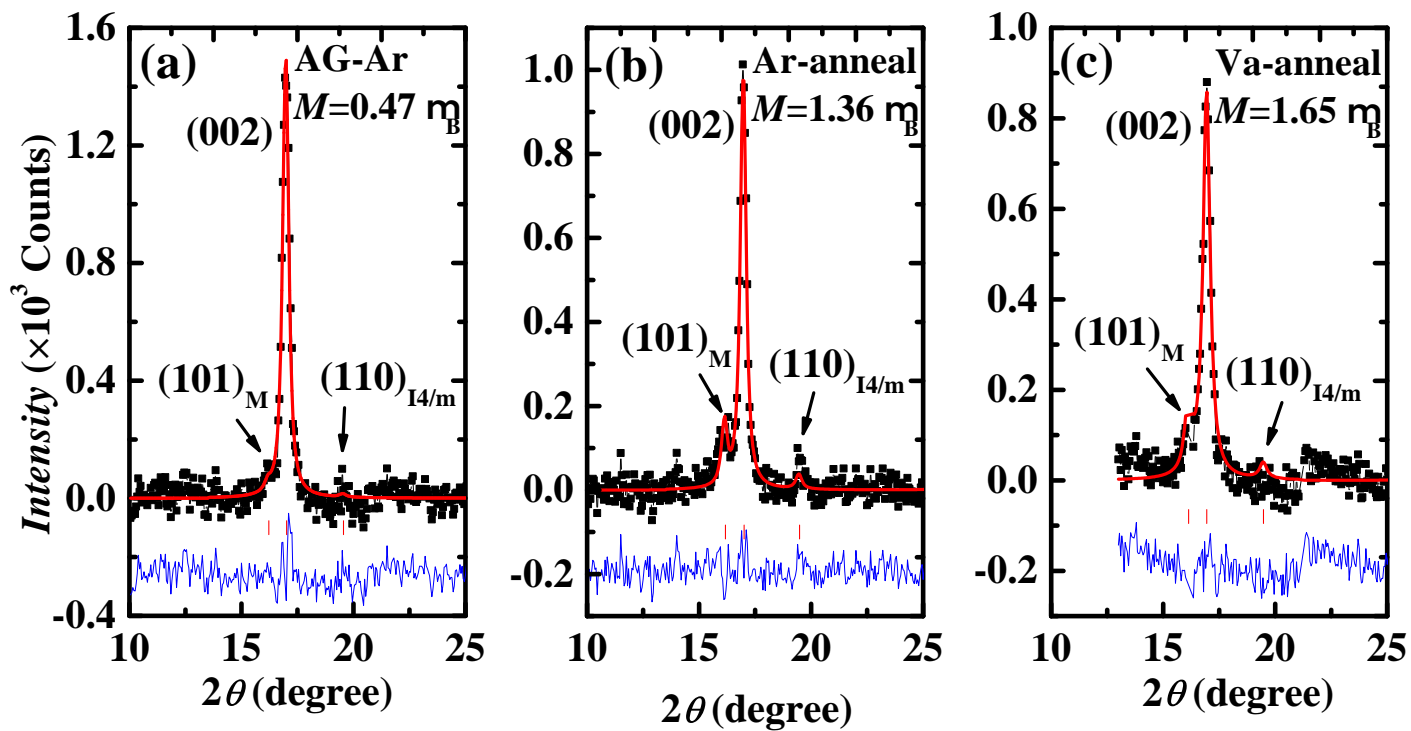


Figure 3, Yang *et al*

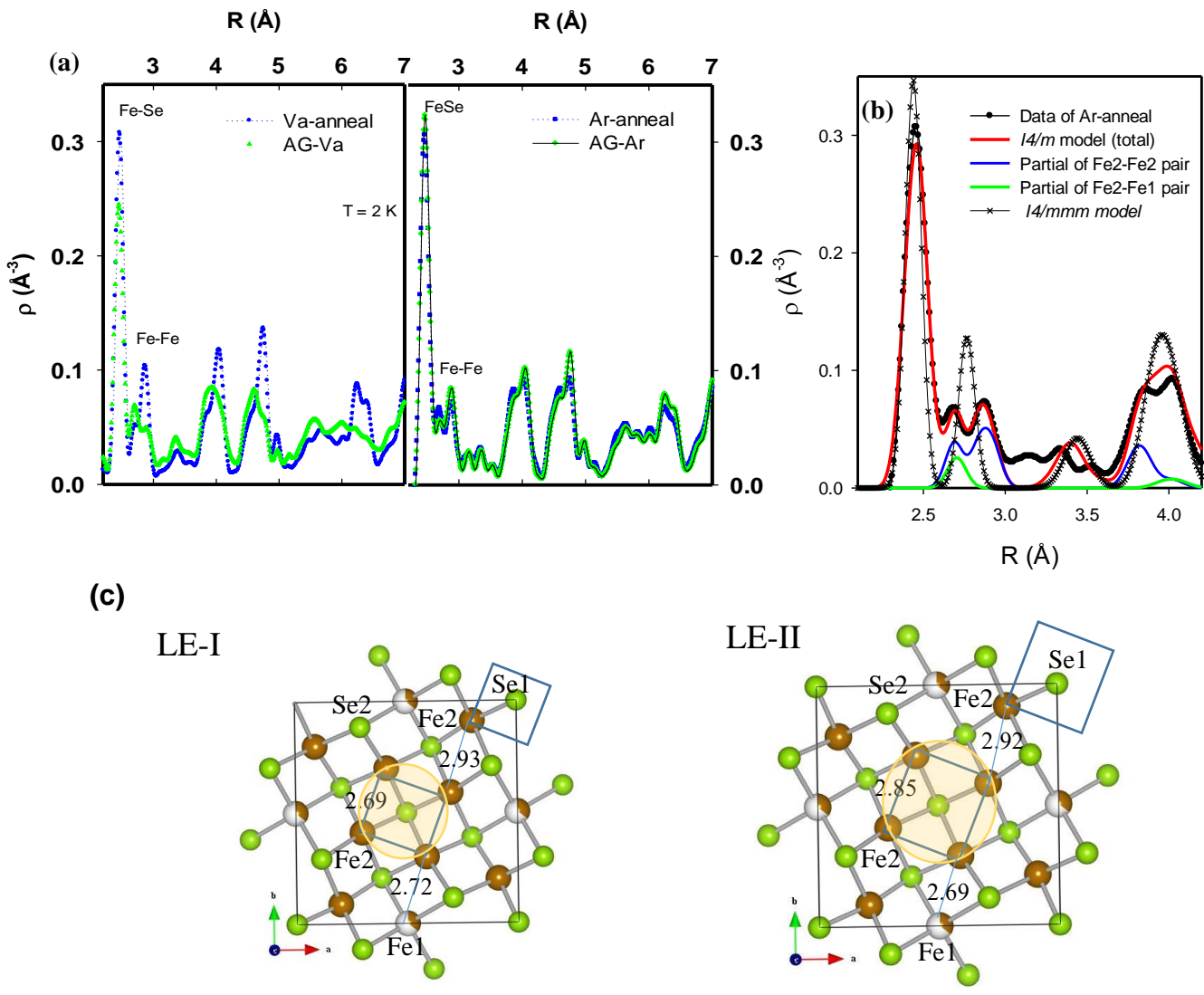


Figure 4, Yang et al.